Nanoscale periodic gradients generated by laser powder bed fusion of an AlSi10Mg alloy

Williams Lefebvre, Gregory Rose, Pauline Delroisse, Eric Baustert, Fabien Cuvilly, Aude Simar

Nanoscale periodic gradients generated by laser powder bed fusion of an AlSi10Mg alloy

Williams Lefebvre[1,*], Grégory Rose[1,2], Pauline Delroisse[3], Eric Baustert[2], Fabien Cuvilly[1], Aude Simar[3]

[1]*Normandie University, UNIROUEN, INSA Rouen, CNRS, Groupe de Physique des Matériaux, 76000 Rouen, France*

[2]*Volum-e, 1 chemin de la fonderie, 76340 Blangy-sur-Bresle, France*

[3] *Institute of Mechanics, Materials and Civil Engineering, UCLouvain, Louvain-la-Neuve, Belgium*

*corresponding author: williams.lefebvre@univ-rouen.fr

Keywords: Laser powder bed fusion, SLM, LPBF, selective laser melting, additive manufacturing powder bed fusion, design, gradient, microstructure, aluminium, Al-Mg-Si, amorphous, clustering, atom probe tomography.

Data availability: the authors confirm that their data are available

Graphical abstract

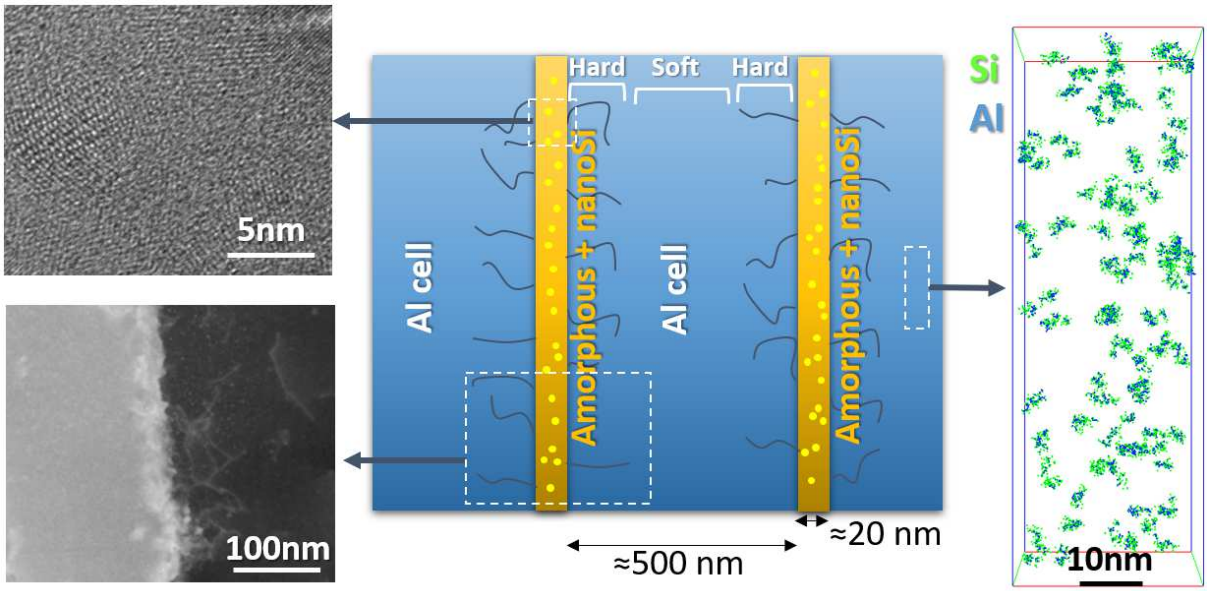

A layered nanostructure is produced by laser powder bed fusion of an Al-Si10Mg alloy. Melt pools are formed of repeated Al cells exhibiting a gradient of dislocation density and nano-layers of amorphous-phase enriched in Al and Si containing fine dispersions of diamond-Si nanocrystals. The high solidification rate involves the formation of a high density of solute-rich clusters in Al crystals.

Abstract

In this study, the formation of a periodic microstructural pattern designed by laser powder bed fusion (LPBF), commonly called selective laser melting (SLM), of an AlSi10Mg alloy is revealed at high resolution using scanning transmission electron microscopy and atom probe tomography. Special attention is paid to the description of non-equilibrium structures and compositional fields resulting from the ultrafast cooling of the LPBF process. Observations reveal the existence of a glass state in eutectic areas, wherein short-range ordering of the diamond-Si structure is observed. The apparent very fast solidification of eutectic regions is found to involve a local strain in adjacent Al cells, which extends up to 100 nm on average. In the supersaturated aluminium solid solution retained by the LPBF process, two populations of clusters are identified, for which the potential role of the selection of hardening phases is discussed. It is proposed that the microstructure of former melt pools outside heat-affected areas is described by the repetition of a periodic microstructural

pattern consisting of eutectic regions /strain-hardened Al-crystals /strain-free Al-crystals with a high density of solute-rich clusters.

1. Introduction

Elaboration of metallic parts by laser powder bed fusion (LPBF) or selective laser melting (SLM) of metallic powders [1–13] offers a unique opportunity to achieve significant hardening by microstructure design. Hardening of alloys is commonly pursued by combining contributions such as lattice friction, solid solution strengthening, work hardening, Hall-Petch strengthening, and precipitation hardening. Insofar as LPBF is applied to produce end products, work hardening cannot be directly considered. Although LPBF is intrinsically a casting process, its advantage comes from the incredibly high cooling rates involved (in the range 10^3–10^6 K/s)[1,14,15]. Whereas similar cooling rates could only be obtained using specific methods such as melt spinning, which produces thin ribbons only [16–18], LPBF allows for the trapping of alloy systems in complex non-equilibrium states, which can also serve as a basis for smart microstructure design by well-defined heat treatments.

Among the aluminium alloys used in additive manufacturing, hypoeutectic alloys are quite common because of their good castability, high strength, and good corrosion resistance [4,19]. Poor ductility and anisotropy are often associated with the as-built condition, which explains why long-duration high-temperature annealing is usually applied to “reset” the microstructure inherited from the LPBF processing [20]. However, in the as-built condition, AlSi10Mg is known to exhibit high tensile strength and hardness compared to the same material processed by conventional casting [20]. Indeed, from the as-built state, interesting properties can already be achieved for Al–Si alloys [12,21,22]. As illustrated in the work by Lien et al. [22], an excellent compromise between the strength and strain can be achieved by means of laser rapid solidification compared to classical casting applied to Al-20wt%Si modified alloys. These authors have clearly shown how the drastic refinement of the microstructure obtained by rapid solidification was responsible for this gain in

strength and ductility.

Accounting for the complex gradients inherited by the LPBF process, advanced material design by heat treatments can be pursued. Physical metallurgists may hence dispose of a complex tangle of regions with significantly different compositions and microstructures at the submicron scale that they can force to evolve to achieve some target properties. In this study, much attention has been paid to the fine-scale characterisation of an AlSi10Mg alloy in the as-built state by a combination of transmission electron microscopy (TEM) and atom probe tomography (APT) analyses. Observations by these two techniques allow for the connection of the non-equilibrium structures to the high cooling rate resulting from the LPBF process. While the repetition of a microstructural pattern in the melt pools is identified, solute clustering in the Al cells is quantitatively investigated, and the potential role of clusters in phase selection during further heat treatments is discussed.

2. Experimental

2.1. Materials elaboration and specimen preparation

Bulk LPBF samples were manufactured on an EOS M290 in the form of plates with dimensions of 150 mm × 35 mm × 5 mm. The build platform was maintained at 35 °C. The choice of this rather low temperature was made to avoid softening and phase decomposition during the process. The fabrication parameters were optimised by the machine manufacturer, which were a laser power of 390 W, powder layer thickness of 30 µm, hatch spacing of 0.19 mm, scanning speed of 1300 mm/s, and rotation between scans rotation of 67°. To prevent sample oxidation during fabrication, the manufacturing chamber was under protective argon gas.

For TEM/scanning TEM (STEM) and APT analyses, samples were prepared by focussed ion beam (FIB) using the *in situ* lift-out technique in a cross-beam NVISION-40 ZEISS. In the first step, a chunk was removed from a bulk sample with milling currents of 6.5 nA and 1.5 nA at 30 kV and welded to a copper grid with a gas injection system, which uses an organometallic gas composed of platinum and

carbon. In the last step, the chunk was machined into a fine lamella with milling currents of 300 pA and 80 pA at 30 kV using Ga ions. To reduce Ga implantation and damage in the region of interest, the final step of milling of the lamella was performed at a low acceleration voltage of 2 kV.

2.2. *Characterisation tools and protocols*

Atom probe experiments were performed using a Cameca LEAP 4000 HR, operating in voltage mode. The voltage pulse fraction was 20% with a pulse repetition rate of 200 kHz, while the specimen temperature was set to 40 K. APT reconstructions and data mining were performed using the IVAS® software. TEM and STEM observations were obtained with a JEOL ARM equipped with a Cs-corrector of the probe forming system. The microscope voltage was set to 200 kV.

In the APT reconstructions, the level of decomposition of the aluminium solid solution was first analysed by plotting radial distribution functions (RDFs) [23,24] An RDF was plotted for a given atom type (e.g. Mg). For each atom of the selected element in the APT reconstruction, the concentrations of all elements in a shell of radius r and thickness dr around the atom were calculated ($C_{Al}(r)$, $C_{Mg}(r)$, $C_{Si}(r)$), and then compared to the average concentration of each of these elements in the whole APT reconstruction by calculating the concentration ratio. Hence, a clustering was indicated by an RDF value > 1, whereas a random distribution of solutes would give a value of 1.

Quantification of clustering in the Al solid solution was performed by applying the maximum separation distance (MSD) algorithm [25,26] extended to high-order nearest neighbour distances, first to Mg atoms and, second, to Si atoms. This well-established cluster search methodology for APT is described and compared with other cluster search methods in several reviews [27–29]. For the sake of clarity and to allow the reader to compare the present results with the literature, the principle and limitations of the method are summarised hereafter.

MSD gathers atoms of selected species in a given cluster if they are closer than the distance d_{max}. Classically, MSD has been applied to first nearest neighbour (1NN) distance distributions in the

literature, and this is also the case in a recent work on an AlSi10Mg alloy elaborated by LPBF [30]. Nevertheless, since 1NN distribution of clusters strongly overlap with the 1NN distribution of the matrix in most cases [30,31], applying d_{max} to 1NN distribution results in the selection of a significant proportion of wrong clusters (corresponding to the "noise" of the algorithm) coming from the start of 1NN distribution in the matrix, together with actual clusters (which are the "signal" of the algorithm). This problem is well documented in the literature with the support of simulations [29,31], and it has been proven that applying a criterion N_{min} on the minimum number of solute atoms per cluster is not sufficient to retrieve a satisfying signal over noise ratio if only the 1NN distance distribution is considered. On the contrary, the reliability of the MSD algorithm is significantly improved by considering KNN (K^{th} nearest neighbour distance) distributions with K>1 [31,32].

Insofar as an arbitrary definition of (K, d_{max},N_{min}) is not expected to lead to optimum values (i.e., maximising the signal-to-noise ratio and providing a fair description of the clusters), a heuristic approach has been used to identify the optimum parameters for the algorithm [32–35]. This is done by comparing the results of cluster selection for numerous sets of parameters (K, d_{max},N_{min}) in the analysed volume and in its equivalent randomised volume wherein atomic positions are randomly exchanged. For cluster selection based on Mg atoms, the signal-to-noise ratio was found to be optimum for K = 5, d_{max}= 1.8 nm, and N_{min} = 21. For cluster selection based on Si atoms, the signal-to-noise ratio was found to be optimum for K = 7, d_{max}= 1.0 nm, and N_{min} = 39. Subsequently, the envelope method [36] was used to associate other atoms to the selected clusters. For this method, the envelope length was set to 1 nm and the erosion distance was 0.7 nm.

3. Results

3.1. Non-equilibrium features in eutectic areas and local strain hardening

After LPBF, the microstructure consists of a superimposition of melt pools containing a succession of Al cells separated by eutectic zones. Over several tens of microns, Al cells may display a

similar crystalline orientation, suggesting that they belong to the same primary dendritic Al crystal. Such observations not reported here are already vastly reported at this scale in many papers [12,21,37,38]. In Figure 1, TEM observations of Al cells and eutectic zones are displayed. The specimens were selected well into the melt pools, away from thermally affected zones that can be generated by the LPBF of superior layers. All observed Al cells in Figure 1 have the same orientation, as revealed by fast Fourier transform (FFT) in high-resolution TEM. Their thickness (i.e., their smallest dimension) is approximately 400 nm. No clear precipitation could be revealed inside the Al cells at this scale, suggesting that cooling was fast enough to avoid long-range diffusion of solute elements and phase separation. On the contrary, a slow cooling rate or reheating of the material would have led to solid-state decomposition in the Al cells, along with the formation of Mg_2Si and/or Si particles predicted by the ternary phase diagram. Furthermore, contrasts due to lattice distortions are visible in the Al cells in the vicinity of eutectic regions. Such distortions (indicated by white arrows in Figure 1(a)) could either be generated by coherency strain across the Al-cell/eutectic zone interface or by the volume variation of the eutectic region at the end of its solidification, which occurs after the rapid formation of Al cells. As will be shown hereafter, eutectic areas do not exhibit a lattice structure that could form a coherent interface with Al cells. Hence, lattice distortions are produced by volume variation during the solidification of eutectic regions. Complex interface structures involving both crystalline and amorphous phases have also been shown to produce dislocations in the literature [39,40]. Such distortions are expected to contribute to the residual stress measured at the microscopic scale [41].

Figure 2(a) shows the observation of a eutectic zone in the high-resolution TEM (HR-TEM). The thickness of the eutectic area trapped between the Al cells is in the range of 10–20 nm. The interface with the Al cells is not well-defined because of the superimposition of phases along the direction of projection. While Moiré fringes are generated by overlaps of the crystalline structure along the specimen thickness, obvious contrasts reveal the presence of nanocrystals and an amorphous phase in the eutectic area.

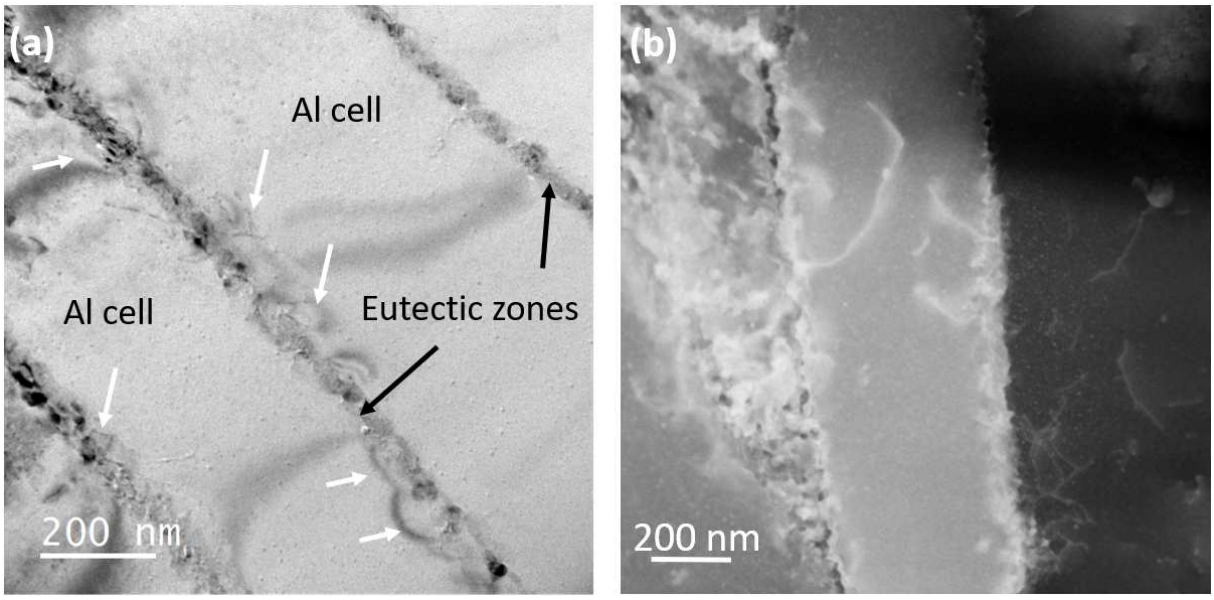

Figure 1 : (a) Bright FieldTEM image displaying Al cells separated by eutectic zones. White arrows point out lattice distortions in the vicinity of eutectic regions. (b) Large-angle annular dark field STEM image showing preferential location of dislocations in Al cells at the vicinity of eutectic regions.

By computing an FFT of the image in Figure 2(a), several spots consistent with the spatial frequency of the {111} planes of diamond Si are identified in Figure 2(b). The random orientation of these reflexions is the signature of equiaxed crystallisation of diamond Si in the eutectic area. By selecting the eutectic area for the calculation of the FFT, it was confirmed that both these spots and the diffuse circle of radius 3.2 nm^{-1} are generated by the eutectic region. Whereas the circle of diffuse intensity is generated by an amorphous structure, the recurrent 3.2 nm^{-1} frequency indicates a local ordering compatible with the formation of {111} planes of diamond Si. This is confirmed by the presence of numerous nanoclusters in Figure 2(c). Insofar as the thickness of the APT specimen rapidly reaches tens of nanometres, direct correlative analysis by APT and HR-TEM becomes inappropriate if the determination of nano-scale features such as those observed in Figure 2(a) is pursued. Hence, the structural analysis of eutectic regions has been determined in thin foils only, and

the distribution of alloying elements in these regions has been investigated in needles analysed by APT.

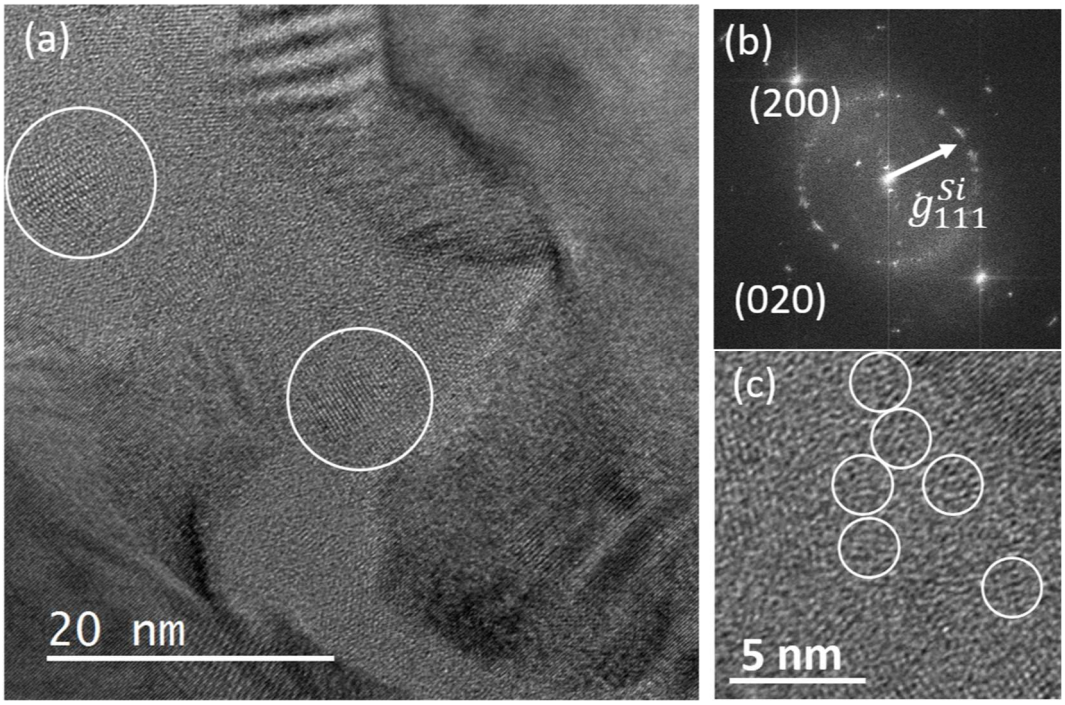

Figure 2 : Al-Si10Mg alloy in the as-built condition. (a) HR-TEM of a eutectic zone surrounded by two Al cells oriented along a [001] zone axis. This region dominated by an amorphous contrast contains nanocrystals as indicated by circles. (b) FFT of the whole image in (a). A diffuse circle of radius 3.2 nm^{-1} consistent with the spatial frequency g_{111}^{Si} associated with (111) planes of Si diamond structure is observed. A discontinuous circle drawn by symmetric spots of similar spatial frequencies is superimposed with the diffuse circle. (c) Enlarged HR-TEM view of the eutectic area. Circles highlight local ordering in the amorphous region.

A eutectic area was intercepted in the APT analysis of a region of interest selected by FIB SEM, and the result is shown in Figure 3. Significant enrichment in Si was visible in the projected volume. Quantification of local composition variations has been performed with respect to this enrichment by first identifying isosurfaces based on the variations in the Si composition. In the APT reconstruction of Figure 3(a), three regions (designated as I, II, and III) are identified. The

composition profiles displayed in Figure 3(b) have been plotted across the interface separating regions II and III in the direction indicated by the arrows in Figure 3(a). Region I shows, with a radius of 2 nm, a Mg:Si ratio > 2 and an Al content of about 20 at%. Such contents are compatible with a Mg_2Si-type precipitate of a non-equilibrium composition. This non-equilibrium composition is associated with the high Al content in the precipitate. Region II is significantly rich in Al, although the level of solute elements (> 30 at%) is incompatible with the composition of an Al cell. It is surrounded by a shell of nearly equiatomic composition in Al and Si (region III), from which the Si and Mg contents gradually decrease as the Al content increases. The APT analysis of a eutectic region confirms that LPBF can generate unusual and non-equilibrium composition variations at the nanometre scale. Phases present along the gradient interface are therefore identified owing to the structural features revealed by high-resolution observations and FFT analysis of Figure 2 and from the additional information provided by the APT analysis. Nano-scale precipitates of diamond Si and Mg_2Si phases are formed in the eutectic region. They are embedded in an amorphous phase, wherein the short-range order of the diamond-Si is revealed. This non-equilibrium amorphous structure is observed in a transient state of decomposition. Region III of Figure 3, which spreads over several nanometres, is perfectly consistent with the local diamond Si short-range order regions highlighted in Figure 2(c). Region II of Figure 3 was consequently identified as the retained amorphous phase.

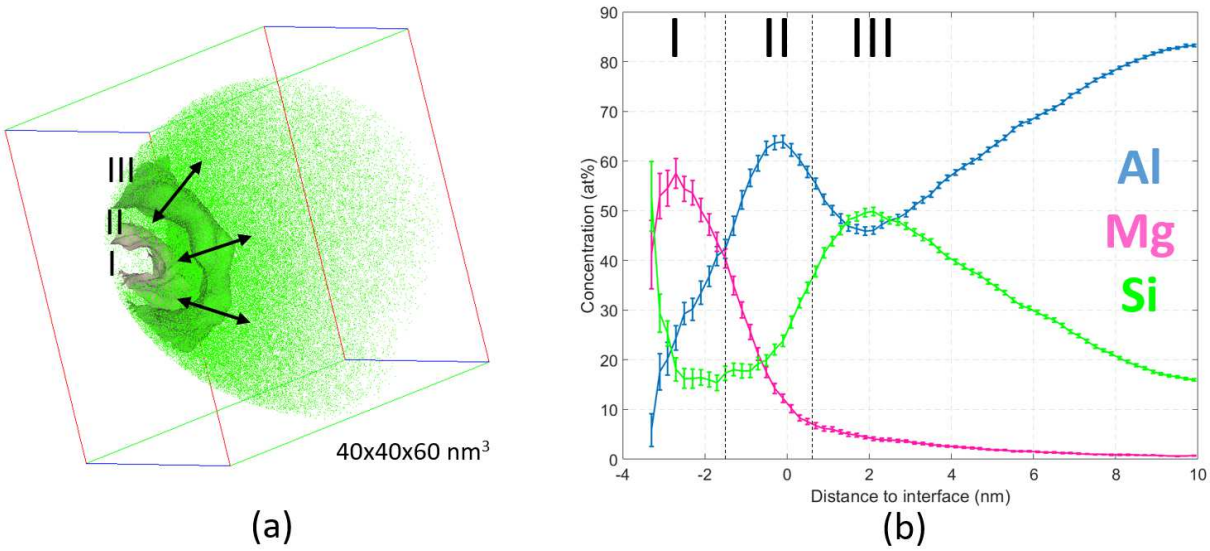

Figure 3 : APT analysis of a eutectic zone in the as-built state. (a) 3D reconstruction displaying only Si atoms (green points) and an isosurface of 25.5 at% of Si (green surface between region II and III). (b) Composition profiles calculated across the Si isosurface shown in (a). Three zones named I, II and III are identified.

3.2. Quantification of clustering in the supersaturated solid solution

APT analyses were performed in the Al cells. The composition of the solid solution is detailed in Table 1. As expected, the rapid cooling undergone by LPBF induces a large supersaturation in the Al cells, and no precipitation could be revealed away from the heat-affected zone. Indeed, Zandbergen et al. showed that the solid solubility of Si and Mg was lower than 0.05 at% below 180 °C [42]. However, the fluctuations of solute distribution in the Al solid solution may be already identified in Figure 4(a) and affect both Mg and Si at a very fine scale. In order to clearly identify and quantify these fluctuations, RDFs [23,24] were calculated in the APT reconstruction of Figure 4 for Mg atoms and Si atoms separately. These are plotted in Figure 5. Around Mg atoms, the composition of Mg is on average significantly higher (up to 3 times higher on average), whereas a significant enrichment in Si can also be distinguished. These enrichments may extend slightly above 2 nm. Around the Si atoms, the solute distribution is also found to be non-random. Nevertheless, it is impossible to conclude from RDF calculations whether local solute enrichments correspond to one or more

populations of clusters. For this purpose, further quantification of clustering has been undertaken using the well-established cluster search methodology described in section 2.2.

Table 1 : Composition of the solid solution of the Al-Si10Mg alloy in the as-built condition

	Al	Si	Mg
Composition (at%)	96.78 ± 0.01	3.08 ± 0.01	0.14 ± 0.01

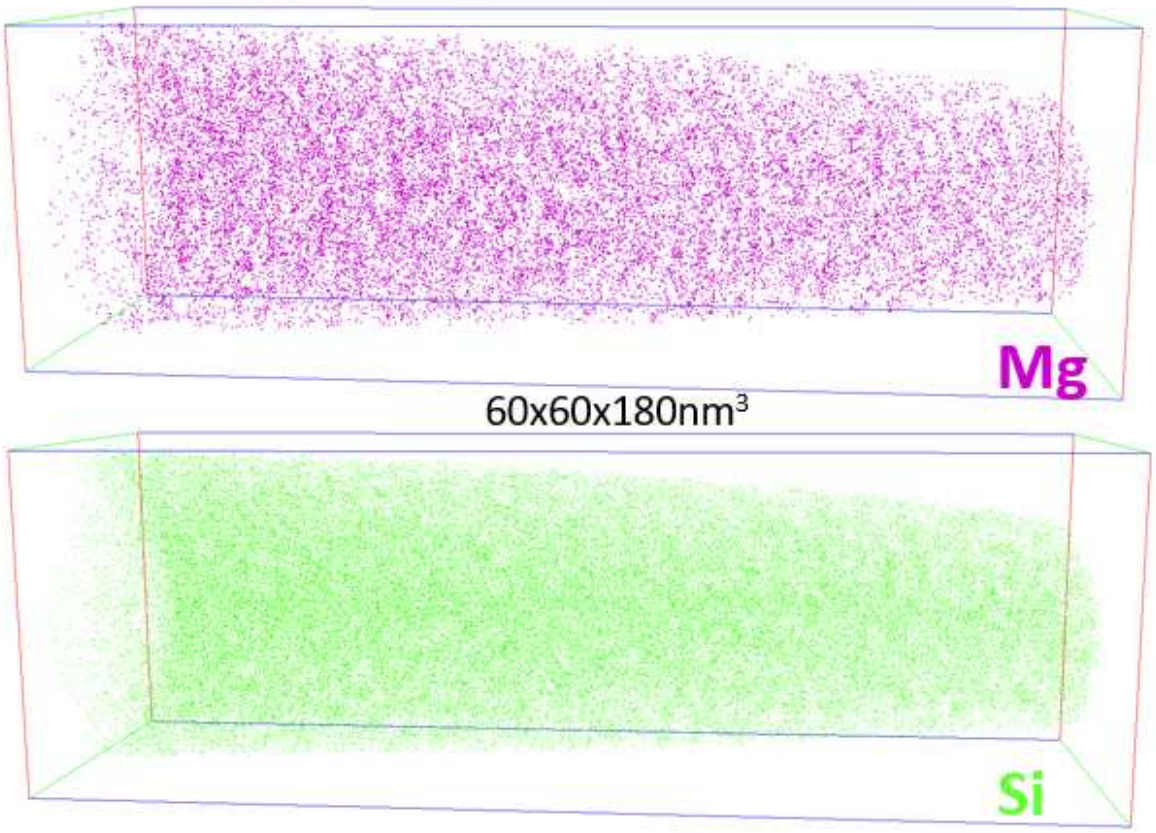

Figure 4 : APT analysis performed in an Al cell of the Al-Si10Mg alloy in the as-built condition. Mg and Si atoms are shown in the APT reconstruction.

In Figure 6(a,b), clusters selected by considering the neighbourhood of Si or Mg atoms are displayed. The Mg:Si ratio as a function of the cluster size in Mg-rich clusters is plotted in Figure 6(c). Although the largest clusters exhibit a Mg:Si ratio close to 2, large discrepancies are observed for

smaller ones, with a significant Mg enrichment in some. On the contrary, Si-rich clusters do not contain Mg atoms in proportions superior to the nominal composition. Consequently, the Mg enrichment shown by the RDF calculated around the Si atoms is attributed to the Si atoms present in the Mg-rich clusters. For comparison, the composition in the Si-rich clusters is plotted as a function of their size, as shown in Figure 6(d). The Si composition is larger than 50 at% on average. This corresponds to a drastic enrichment compared to the average content of Si in the solid solution (~3 at% from Table 1).

(a)

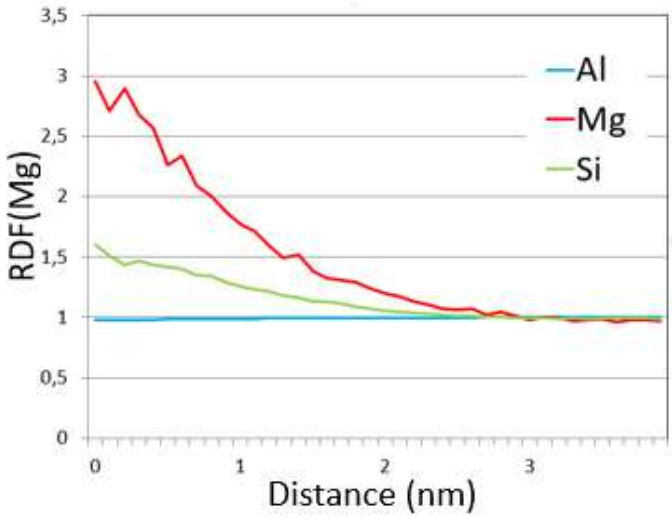

(b)

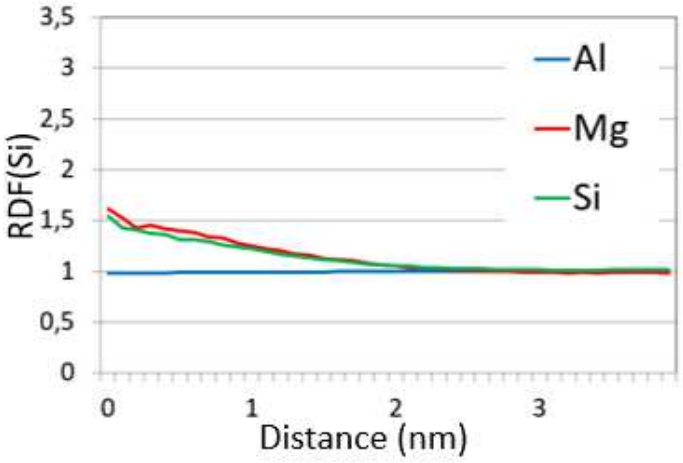

Figure 5 : Radial distribution functions calculated around (a) Mg or (b) Si atoms extracted from an APT analysis performed in an Al cell of the Al-Si10Mg alloy in the as-built condition.

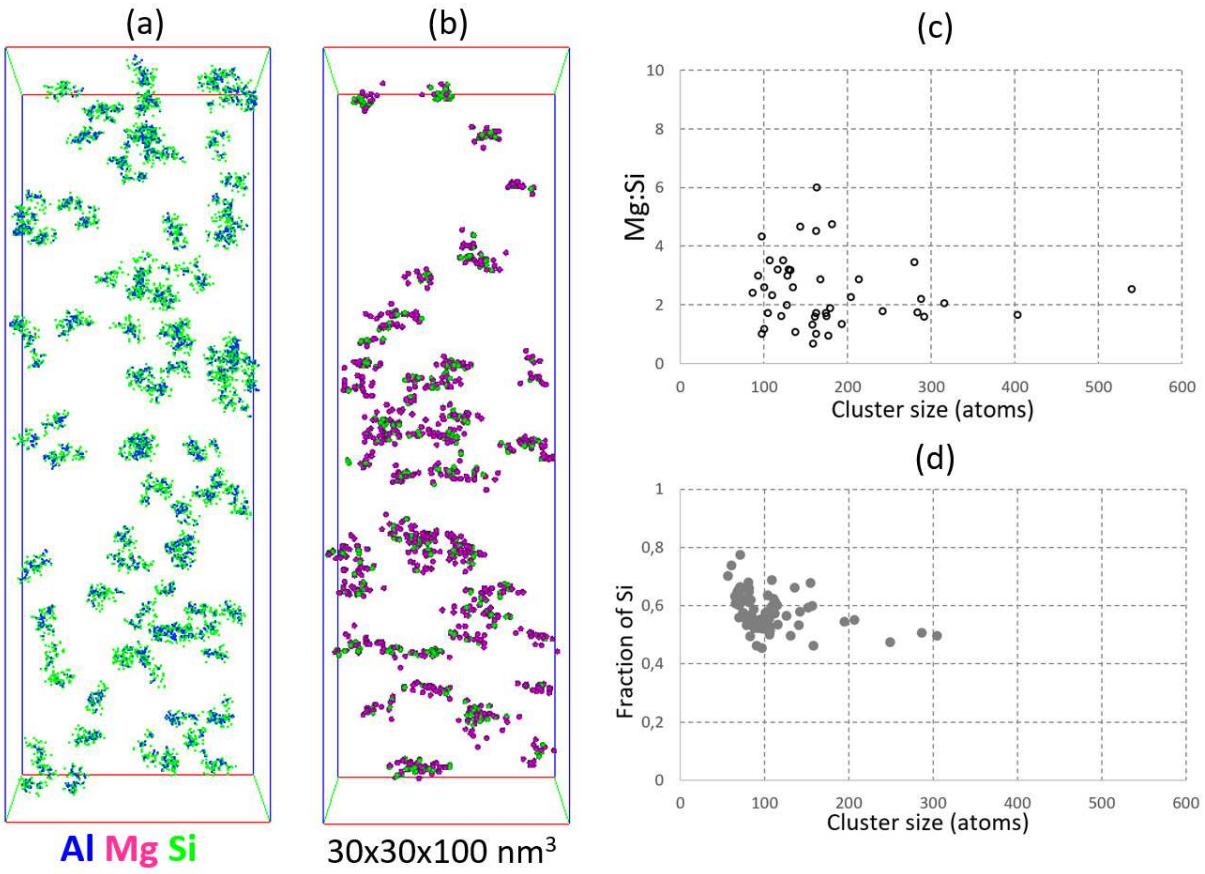

Figure 6 : Solute clusters selected by the cluster search algorithm applied on Si atoms (a) and Mg atoms (b) extracted from APT data. (c) Mg:Si ratio in clusters shown in (b). (d) Fraction of Si in clusters shown in (a).

Finally, the number densities of the two populations of clusters were calculated and are displayed in Table 2. The measured values are typically one order of magnitude larger than values reported in the literature of 6xxx wrought alloys (see, for instance, [42,43]). One can also notice that we detect two more Si clusters (free of Mg) than Mg-rich clusters (containing Si). Although Si contributes to both populations of clusters, the larger number density of Si-rich clusters is consistent with the much larger supersaturation in Si in the solid solution compared to the supersaturation in Mg.

Table 2 : Number densities of solute-rich clusters in the as-built state of the AlSi10Mg alloy

	Mg-rich clusters	**Si-rich clusters**

Number density (m^{-3})	(4.9±0.5) 10^{23}	(8.9±0.9) 10^{23}

4. Discussion

In this study, a complex periodic microstructure of AlSi10Mg designed by LPBF is described. Observations have been focussed on the microstructures formed in regions where the cooling rate is expected to be maximum and where no evidence of reheating (by melting of superior layers) was provided. In addition, much attention has been paid to detail both the composition and structure of the eutectic regions at high resolution. In the literature, the characterisation of eutectic regions of Al–Si alloys in the as-built state more often provide two-dimensional chemical mappings by energy dispersive x-ray spectroscopy coupled with SEM, TEM, or STEM observations [44–47]. Although significant microstructural information was revealed by these techniques (cell size, texture, eutectic decomposition, etc.), APT is necessary to detect the fine-scale distribution of elements induced by the LBPF process at the nanometre scale. In addition, it is mandatory to compare the information accessible by APT with observations at the same scale using (S)TEM to relate compositional variations to the structure of the material. By combining these techniques, new information is provided in the present work that highlights the potential of microstructural design of alloys by LPBF.

First, it is demonstrated that LPBF allows trapping of the AlSi10Mg system in an amorphous state in eutectic regions. This is clearly attributed to the very fast cooling associated with the LPBF elaboration process. Similarly, in the case of surface laser processing, the formation of amorphous phases has also been reported and attributed to the short existing time of the melt pool [39,48]. The amorphous matrix observed at high resolution contains large concentrations of both Al and Si, as indicated by the composition profiles in Figure 3. However, more indications about the eutectic regions were given by APT: i) Mg and Si composition varied gradually from the core of the eutectic region towards the surrounding Al cell; ii) composition profiles are not consistent with equilibrium compositions predicted by the phase diagram of the Al–Mg–Si system. Correlating these APT results

with HR-TEM observations confirm that, in eutectic regions, fast cooling enables rapid crystalline ordering at the nanometre scale, accompanied by insufficient long-range diffusion of solute elements. Inside the amorphous matrix, phase separation is shown to start by a short-range ordering compatible with the diamond-Si structure. Some Si nanocrystals are indeed visible in the HR-TEM. APT analysis of a eutectic region also revealed a local enrichment consistent with the formation of a Mg_2Si precipitate. Nevertheless, as they are likely to form without any specific orientation with respect to the Al cells, they are not expected to give any obvious contrast in TEM unless their long axis is by chance oriented along the direction of observation. Short-range diffusion therefore enables the start of a solid-state decomposition, which is rapidly stopped during the LPBF process. The fast cooling rate, thus, locally retains a nanostructure, which is usually obtained by methods that enable high cooling rates such as melt spinning [16–18].

The contraction associated with the rapid solidification of eutectic areas is shown to involve local strain hardening in adjacent Al cells, as shown in Figure 1. This strain hardening was observed locally in the direct vicinity of eutectic zones and was not found to extend to more than 100 nm distant from eutectic zones on average. This local strain of Al cells at the location of the Al-cell/eutectic region interface was systematic in our observations. Inside a melt pool, this results in the formation of a repeated pattern consisting of a eutectic area surrounded by Al crystals, for which the level of strain hardening gradually decreases towards their core.

Inside the Al-cells investigated by APT, a significant supersaturation of the solid solution was observed (Table 1), in agreement with previous works [30,49]. In their paper [30], Maeshima and Oh-ishi investigated the solid solution of an AlSi10Mg alloy. By applying the MSD algorithm, they found that clustering mainly concerned Mg atoms, whereas Si was not found to form either Si clusters or to participate in Mg clusters. Nevertheless, based on their calculation of first nearest neighbours only, this quantification was inevitably strongly affected by a low signal-to-noise ratio, as discussed in detail in some reference work and reviews on the topic [27,31,50] and in the experimental section

above. In the present work, by following a well-established heuristic protocol for cluster selection [32,35,51,52], the type of clusters present in the solid solution in the as-built condition has been clearly established. Cluster analysis revealed that two populations of clusters exist: i) Mg–Si co-clusters with a Mg:Si ratio equal to 2 or above, and ii) Si-rich clusters free of Mg, with a Si content above 50 at%. These findings confirm that, despite the rapid cooling rate intrinsic to LPBF, short-range clustering already occurs in the supersaturated solution of Al cells.

The presence of these clusters obviously plays an important role in the further precipitation of hardening phases if the microstructure is later submitted to a T5-type heat treatment, that is, involving no prior solution treatment but just a low-temperature ageing. Mg-rich clusters are expected to promote the formation of the equilibrium β-Mg_2Si phase predicted by the ternary phase diagram. Meanwhile, the Si-rich clusters, which are twice the number of Mg-rich clusters, are expected to favour the formation of diamond-Si, as predicted by the ternary phase diagram. Moreover, if a heat treatment is applied at moderate temperature (i.e., in the 120–170 °C range) with or without pre-ageing (i.e., below 100 °C), a sequence of metastability implying the formation of Guinier Preston-zones or β'' precipitates could be observed [42,43,53,54]. Hence, a T5-type heat treatment may result in precipitation hardening, involving precipitates commonly observed in the Al–Mg–Si system (i.e., β'', β', or β-Mg_2Si) together with diamond-Si particles, which formation will be favoured by the existence of Si nanocrystals in eutectic regions and Si-rich clusters in the matrix. A detailed and systematic study of precipitation hardening kinetics starting from the as-built condition, which falls outside the scope of this paper, are required to reveal the hierarchy of phases to be formed and the associated mechanical properties for T5-type hardening treatments. It must also be mentioned that T5-type heat treatments have already been shown to produce significant hardening compared to T6-type heat treatments (involving a prior solution heat treatment) in other alloy systems [55].

Insofar as processing parameters may play a critical role in the final designed microstructure, further investigations are required to identify the exact correlations between these parameters and

the particular microstructural features revealed by this work. These include the existence of an amorphous phase together with Si nanocrystals in eutectic regions and the strain regions in Al cells in the vicinity of eutectic regions. As a particularly important parameter, the temperature of the platform was set to 35 °C to avoid significant phase decomposition and softening, which are expected to occur if this temperature is raised to 180–200 °C, as would typically be done to minimise residual stress in large pieces of material in the as-built state. A low temperature of the platform clearly promotes a high cooling rate and formation on nano-scale periodic gradients, but may be detrimental for residual stress [56].

5. Conclusion

Elaboration of alloys by means of SLM/LBPF offers new ways to guide the microstructural design. One of the main advantages of this method is its high cooling rate, which allows the trapping of alloy systems in non-equilibrium states. Such states can later serve as the basis of smart design using further heat treatments or can lead to unusual properties in the as-built state. In this study, the fine microstructure inherited by the LPBF of an AlSi10Mg alloy was investigated. By means of various microscopy tools, the repetition of a periodicity has been revealed, which implies several scales (from hundreds of nanometres for Al cells to atomic clusters). High-resolution observations have revealed the existence of a glass state in eutectic areas, wherein short-range ordering of the diamond-Si structure could be observed. In these eutectic regions, early stages of phase separation could also be demonstrated by the presence of Si nanocrystals and by the existence of complex compositional fields determined by APT. The apparent very fast solidification of eutectic regions is found to involve a local strain in adjacent Al cells, which extends up to 100 nm on average. The recurrence of this observation produces the repetition of a periodic pattern inside former melt pools (eutectic regions first, surrounded by strain-hardened Al crystals, followed by strain-free Al crystals).

The supersaturated aluminium solid solution retained by the LPBF process was quantitatively investigated by APT. Two populations of clusters were identified: Mg/Si co-clusters and Mg-free Si clusters. Determining the role that these clusters may play in the selection of phases and on subsequent hardening during a precipitation treatment (T5 type) would require further investigation.

Acknowledgements

P. Delroisse acknowledges the financial support of the FRIA, Belgium. A. Simar acknowledges the European Research Council (ERC) under the European Union's Horizon 2020 research and innovation program (grant agreement n716678). Juan Guillermo Santos Macías is acknowledged for providing the LPBF samples from his PhD thesis and useful discussions about them.

References

[1] X.P. Li, G. Ji, Z. Chen, A. Addad, Y. Wu, H.W. Wang, J. Vleugels, J. Van Humbeeck, J.P. Kruth, Selective laser melting of nano-TiB2decorated AlSi10Mg alloy with high fracture strength and ductility, Acta Mater. 129 (2017) 183–193. https://doi.org/10.1016/j.actamat.2017.02.062.

[2] J.P. Kruth, P. Mercelis, J. Van Vaerenbergh, L. Froyen, M. Rombouts, Binding mechanisms in selective laser sintering and selective laser melting, Rapid Prototyp. J. 11 (2005) 26–36. https://doi.org/10.1108/13552540510573365.

[3] M.G. Rashed, M. Ashraf, R.A.W. Mines, P.J. Hazell, Metallic microlattice materials: A current state of the art on manufacturing, mechanical properties and applications, Mater. Des. 95 (2016) 518–533. https://doi.org/10.1016/j.matdes.2016.01.146.

[4] E.O. Olakanmi, R.F. Cochrane, K.W. Dalgarno, A review on selective laser sintering/melting (SLS/SLM) of aluminium alloy powders: Processing, microstructure, and properties, Prog. Mater. Sci. 74 (2015) 401–477. https://doi.org/10.1016/j.pmatsci.2015.03.002.

[5] J.H. Martin, B.D. Yahata, J.M. Hundley, J.A. Mayer, T.A. Schaedler, T.M. Pollock, 3D printing of high-strength aluminium alloys, Nature. 549 (2017) 365–369. https://doi.org/10.1038/nature23894.

[6] C.Y. Yap, C.K. Chua, Z.L. Dong, Z.H. Liu, D.Q. Zhang, L.E. Loh, S.L. Sing, Review of selective laser melting: Materials and applications, Appl. Phys. Rev. 2 (2015). https://doi.org/10.1063/1.4935926.

[7] L. Thijs, F. Verhaeghe, T. Craeghs, J. Van Humbeeck, J.P. Kruth, A study of the microstructural evolution during selective laser melting of Ti-6Al-4V, Acta Mater. 58 (2010) 3303–3312. https://doi.org/10.1016/j.actamat.2010.02.004.

[8] E. Louvis, P. Fox, C.J. Sutcliffe, Selective laser melting of aluminium components, J. Mater. Process. Technol. 211 (2011) 275–284. https://doi.org/10.1016/j.jmatprotec.2010.09.019.

[9] I. Yadroitsev, P. Bertrand, I. Smurov, Parametric analysis of the selective laser melting process, Appl. Surf. Sci. 253 (2007) 8064–8069. https://doi.org/10.1016/j.apsusc.2007.02.088.

[10] W. Van den Broek, S. Van Aert, D. Van Dyck, A model based reconstruction technique for depth sectioning with scanning transmission electron microscopy, Ultramicroscopy. 110 (2010) 548–554. https://doi.org/10.1016/j.ultramic.2009.09.008.

[11] N.T. Aboulkhair, N.M. Everitt, I. Ashcroft, C. Tuck, Reducing porosity in AlSi10Mg parts processed by selective laser melting, Addit. Manuf. 1 (2014) 77–86. https://doi.org/10.1016/j.addma.2014.08.001.

[12] E. Brandl, U. Heckenberger, V. Holzinger, D. Buchbinder, Additive manufactured AlSi10Mg samples using Selective Laser Melting (SLM): Microstructure, high cycle fatigue, and fracture behavior, Mater. Des. 34 (2012) 159–169. https://doi.org/10.1016/j.matdes.2011.07.067.

[13] K.N. Amato, S.M. Gaytan, L.E. Murr, E. Martinez, P.W. Shindo, J. Hernandez, S. Collins, F. Medina, Microstructures and mechanical behavior of Inconel 718 fabricated by selective laser melting, Acta Mater. 60 (2012) 2229–2239. https://doi.org/10.1016/j.actamat.2011.12.032.

[14] M. Qian, W. Xu, M. Brandt, H.P. Tang, Additive manufacturing and postprocessing of Ti-6Al-4V for superior mechanical properties, MRS Bull. 41 (2016) 775–783. https://doi.org/10.1557/mrs.2016.215.

[15] H.Y. Jung, S.J. Choi, K.G. Prashanth, M. Stoica, S. Scudino, S. Yi, U. Kühn, D.H. Kim, K.B. Kim, J. Eckert, Fabrication of Fe-based bulk metallic glass by selective laser melting: A parameter study, Mater. Des. 86 (2015) 703–708. https://doi.org/10.1016/j.matdes.2015.07.145.

[16] A. Bendijk, R. Delhez, L. Katgerman, T.H. De Keijser, E.J. Mittemeijer, N.M. Van Der Pers, Characterization of Al-Si-alloys rapidly quenched from the melt, J. Mater. Sci. 15 (1980) 2803–2810. https://doi.org/10.1007/BF00550549.

[17] K. Hono, K. Hiraga, Q. Wang, A. Inoue, T. Sakurai, The microstructure evolution of a Fe73.5Si13.5B9Nb3Cu1 nanocrystalline soft magnetic material, Acta Metall. Mater. 40 (1992) 2137–2147. https://doi.org/10.1016/0956-7151(92)90131-W.

[18] W. Lefebvre, S. Morin-Grognet, F. Danoix, Role of Niobium in the nanocrystallization of a Fe73.5Si13.5B9Nb3Cu alloy, J. Magn. Magn. Mater. 301 (2006). https://doi.org/10.1016/j.jmmm.2005.07.008.

[19] R.X. Li, R.D. Li, Y.H. Zhao, L.Z. He, C.X. Li, H.R. Guan, Z.Q. Hu, Age-hardening behavior of cast Al-Si base alloy, Mater. Lett. 58 (2004) 2096–2101. https://doi.org/10.1016/j.matlet.2003.12.027.

[20] E. Padovano, C. Badini, A. Pantarelli, F. Gili, F. D'Aiuto, A comparative study of the effects of thermal treatments on AlSi10Mg produced by laser powder bed fusion, J. Alloys Compd. 831 (2020) 154822. https://doi.org/10.1016/j.jallcom.2020.154822.

[21] L. Thijs, K. Kempen, J.P. Kruth, J. Van Humbeeck, Fine-structured aluminium products with controllable texture by selective laser melting of pre-alloyed AlSi10Mg powder, Acta Mater. 61 (2013) 1809–1819. https://doi.org/10.1016/j.actamat.2012.11.052.

[22] H.-H. Lien, J. Mazumder, J. Wang, A. Misra, Ultrahigh strength and plasticity in laser rapid solidified Al–Si nanoscale eutectics, Mater. Res. Lett. 8 (2020) 291–298. https://doi.org/10.1080/21663831.2020.1755380.

[23] C.K. Sudbrack, R.D. Noebe, D.N. Seidman, Direct observations of nucleation in a nondilute multicomponent alloy, Phys. Rev. B - Condens. Matter Mater. Phys. 73 (2006) 212101. https://doi.org/10.1103/PhysRevB.73.212101.

[24] E.A. Marquis, PhD Thesis, Northwestern University, 2002, n.d.

[25] J.M. Hyde, PhD dissertation. Oxford: University of Oxford (1993)., n.d.

[26] J.M. Hyde, C.A. English, An Analysis of the Structure of Irradiation induced Cu-enriched Clusters in Low and High Nickel Welds, MRS Proc. 650 (2000) R6.6. https://doi.org/10.1557/PROC-650-R6.6.

[27] E.A. Marquis, J.M. Hyde, Applications of atom-probe tomography to the characterisation of solute behaviours, Mater. Sci. Eng. R Reports. 69 (2010) 37–62. https://doi.org/10.1016/j.mser.2010.05.001.

[28] W. Lefebvre-Ulrikson, F. Vurpillot, X. Sauvage, Atom probe tomography put theory into

practice, Academic Press, 2016.

[29] B. Gault, M.P. Moody, J.M. Cairney, S.P. Ringer, Atom Probe Microscopy, Springer Ser. Mater. Sci. (2012) 396. https://doi.org/10.1007/978-0-387-73068-4.

[30] T. Maeshima, K. Oh-ishi, Solute clustering and supersaturated solid solution of AlSi10Mg alloy fabricated by selective laser melting, Heliyon. 5 (2019) e01186. https://doi.org/10.1016/j.heliyon.2019.e01186.

[31] W. Lefebvre-Ulrikson, G. Da Costa, L. Rigutti, I. Blum, Data Mining, in: Atom Probe Tomogr. Put Theory Into Pract., Elsevier Inc., 2016: pp. 279–317. https://doi.org/10.1016/B978-0-12-804647-0.00009-7.

[32] L.T. Stephenson, Cluster analysis under microscope: quantitative techniques for atom probe analysis of solute clustering in multi-component materials, Ph Dissertation, The University of Sydney, NSW 2006, Australia, 2009.

[33] M.K. Miller, B.D. Wirth, G.R. Odette, Precipitation in neutron-irradiated Fe–Cu and Fe–Cu–Mn model alloys: a comparison of APT and SANS data, Mater. Sci. Eng. A. 353 (2003) 133–139. https://doi.org/10.1016/S0921-5093(02)00679-2.

[34] D. Vaumousse, A. Cerezo, P.J. Warren, A procedure for quantification of precipitate microstructures from three-dimensional atom probe data, Ultramicroscopy. 95 (2003) 215–221. https://doi.org/10.1016/S0304-3991(02)00319-4.

[35] R.P. Kolli, D.N. Seidman, Comparison of compositional and morphological atom-probe tomography analyses for a multicomponent Fe-Cu steel, Microsc. Microanal. 13 (2007) 272–84. https://doi.org/10.1017/S1431927607070675.

[36] M.K. Miller, E.A. Kenik, Atom probe tomography: a technique for nanoscale characterization., Microsc. Microanal. 10 (2004) 336–41. https://doi.org/10.1017/S1431927604040577.

[37] R. Casati, M. Vedani, Aging Response of an A357 Al Alloy Processed by Selective Laser Melting, Adv. Eng. Mater. 21 (2019) 1800406. https://doi.org/10.1002/adem.201800406.

[38] P. Delroisse, P.J. Jacques, E. Maire, O. Rigo, A. Simar, Effect of strut orientation on the microstructure heterogeneities in AlSi10Mg lattices processed by selective laser melting, Scr. Mater. 141 (2017) 32–35. https://doi.org/10.1016/j.scriptamat.2017.07.020.

[39] J. Li, Z. Ye, C. Jing, S. Xu, F. Yu, K. Liu, X. Sun, S. Liu, F. Cao, L. Liu, X. Wang, Surface reinforcements of TA15 titanium alloy with laser induced Co base multiphase composites,

Opt. Laser Technol. 132 (2020) 106480. https://doi.org/10.1016/j.optlastec.2020.106480.

[40] J. Li, Z. Ye, J. Fu, W. Qi, Y. Tian, L. Liu, X. Wang, Microstructure evolution, texture and laser surface HEACs of Al-Mg-Si alloy for light automobile parts, Mater. Charact. 160 (2020) 110093. https://doi.org/10.1016/j.matchar.2019.110093.

[41] N.C. Levkulich, S.L. Semiatin, J.E. Gockel, J.R. Middendorf, A.T. DeWald, N.W. Klingbeil, The effect of process parameters on residual stress evolution and distortion in the laser powder bed fusion of Ti-6Al-4V, Addit. Manuf. 28 (2019) 475–484. https://doi.org/10.1016/j.addma.2019.05.015.

[42] M.W. Zandbergen, Q. Xu, A. Cerezo, G.D.W. Smith, Data analysis and other considerations concerning the study of precipitation in Al-Mg-Si alloys by Atom Probe Tomography, Data Br. 5 (2015) 626–641. https://doi.org/10.1016/j.dib.2015.09.045.

[43] M. Torster, H.S. Hasting, W. Lefebvre, C.D. Marioara, J.C. Walmsley, S.J. Andersen, R. Holmestad, The influence of composition and natural aging on clustering during preaging in Al-Mg-Si alloys, J. Appl. Phys. 108 (2010). https://doi.org/10.1063/1.3481090.

[44] H. Rao, S. Giet, K. Yang, X. Wu, C.H.J. Davies, The influence of processing parameters on aluminium alloy A357 manufactured by Selective Laser Melting, Mater. Des. 109 (2016) 334–346. https://doi.org/10.1016/j.matdes.2016.07.009.

[45] B. Chen, S.K. Moon, X. Yao, G. Bi, J. Shen, J. Umeda, K. Kondoh, Strength and strain hardening of a selective laser melted AlSi10Mg alloy, Scr. Mater. 141 (2017) 45–49. https://doi.org/10.1016/j.scriptamat.2017.07.025.

[46] C. Yan, L. Hao, A. Hussein, P. Young, J. Huang, W. Zhu, Microstructure and mechanical properties of aluminium alloy cellular lattice structures manufactured by direct metal laser sintering, Mater. Sci. Eng. A. 628 (2015) 238–246. https://doi.org/10.1016/j.msea.2015.01.063.

[47] J. Wu, X.Q. Wang, W. Wang, M.M. Attallah, M.H. Loretto, Microstructure and strength of selectively laser melted AlSi10Mg, Acta Mater. 117 (2016) 311–320. https://doi.org/10.1016/j.actamat.2016.07.012.

[48] J. Li, Y. Tian, L. Zhang, X. Wang, X. Wang, Laser/argon-arc strengthening of titanium alloy surface with Deloro matrix composites, Opt. Laser Technol. 123 (2020) 105911. https://doi.org/10.1016/j.optlastec.2019.105911.

[49] X.P. Li, X.J. Wang, M. Saunders, A. Suvorova, L.C. Zhang, Y.J. Liu, M.H. Fang, Z.H. Huang, T.B.

Sercombe, A selective laser melting and solution heat treatment refined Al-12Si alloy with a controllable ultrafine eutectic microstructure and 25% tensile ductility, Acta Mater. 95 (2015) 74–82. https://doi.org/10.1016/j.actamat.2015.05.017.

[50] L.T. Stephenson, M.P. Moody, S.P. Ringer, Theory of Solute Clustering in Materials for Atom Probe, Philos. Mag. 91 (2011) 2200–2215. https://doi.org/10.1080/14786435.2011.554909.

[51] R.K.W. Marceau, L.T. Stephenson, C.R. Hutchinson, S.P. Ringer, Quantitative atom probe analysis of nanostructure containing clusters and precipitates with multiple length scales., Ultramicroscopy. 111 (2011) 738–42. https://doi.org/10.1016/j.ultramic.2010.12.029.

[52] W. Lefebvre-Ulrikson, Correlative Microscopy by (Scanning) Transmission Electron Microscopy and Atom Probe Tomography, in: Atom Probe Tomogr., Elsevier, 2016: pp. 319–351. https://doi.org/10.1016/B978-0-12-804647-0.00010-3.

[53] G. a. Edwards, K. Stiller, G.L. Dunlop, M.J. Couper, The precipitation sequence in Al–Mg–Si alloys, Acta Mater. 46 (1998) 3893–3904. https://doi.org/10.1016/S1359-6454(98)00059-7.

[54] F. De Geuser, W. Lefebvre, D. Blavette, 3D atom probe investigation of the early stages of precipitation in an Al-Mg-Si alloy, in: Proc. an Int. Conf. Solid-Solid Phase Transform. Inorg. Mater. 2005, 2005.

[55] M.L. Montero Sistiaga, R. Mertens, B. Vrancken, X. Wang, B. Van Hooreweder, J.P. Kruth, J. Van Humbeeck, Changing the alloy composition of Al7075 for better processability by selective laser melting, J. Mater. Process. Technol. 238 (2016) 437–445. https://doi.org/10.1016/j.jmatprotec.2016.08.003.

[56] L. Zhao, J.G. Santos Macías, A. Dolimont, A. Simar, E. Rivière-Lorphèvre, Comparison of residual stresses obtained by the crack compliance method for parts produced by different metal additive manufacturing techniques and after friction stir processing, Addit. Manuf. 36 (2020) 101499. https://doi.org/10.1016/j.addma.2020.101499.